High Temperature Corrosion of Materials (2026) 103:40
https://doi.org/10.1007/s11085-026-10399-x

RESEARCH

Theoretical Insights into the Anti-Corrosion Effectiveness of Indole-Based Compounds on Surfaces of Iron: An Integrated DFT Along with Monte Carlo Simulations Studies

Rebaz Obaid Kareem[1] · Kareem Jumaah Al-Salihi[2] · Rebaz Anwar Omer[3] · Yousif Hussein Azeez[1] · Lana Omer Ahmed[4] · Muhammad Ashfaq[5] · Senem Akkoc[6,7] · Aseel Smerat[8,9] · Mehran Feizi-Dehnayebi[6]

Received: 10 February 2026 / Revised: 15 April 2026 / Accepted: 20 April 2026
© The Author(s) 2026

Abstract

Corrosion of metal surfaces remains a persistent challenge across industrial environments, necessitating the exploration of efficient and eco-friendly inhibitors. The aim and novelty of present study is the comprehensive theoretical investigation of ten indole-based derivatives (**ST1–ST10**) as corrosion inhibitors efficiency for Fe surfaces. Using DFT at the B3LYP/6–311 ++ G(2d,p), we computed key electronic properties such as HOMO–LUMO energies, dipole moments, to assess molecular stability and reactivity. Natural Bond Orbital (NBO) analysis identified strong $\pi \rightarrow \pi^*$, $\sigma \rightarrow \sigma^*$, and $LP \rightarrow \pi^*$ delocalization, confirming notable electron mobility within molecular frameworks. To sum, the chemical softness values show that the title compounds **ST8** and **ST10** preferentially exchange their associated electron clouds with the surrounding environment. These findings offer a robust multiscale framework for designing advanced indole-based inhibitors for corrosion protection in aggressive environments.

Keywords Indole derivatives · DFT · MC · NBO · Adsorption energy

Introduction

Organic substances are known for their peculiar structural characteristics, particularly heterocyclic compounds or substances with heteroatoms like oxygen, phosphorus, sulfur, and nitrogen [1]. The prominent characteristics of heterocyclic compounds are aromaticity and planarity which enhance stability of that class of compounds [2], more polar than homocyclic compounds which enable them to have higher dipole moment, and ability to act as versatile ligands to form numerous metal

Extended author information available on the last page of the article

Published online: 07 May 2026

complexes [3, 4]. Since most naturally occurring compounds are heterocyclic, therefore the study of heterocyclic compounds has received a lot of interest. Among them, indole-based compounds are particularly notable because of their numerous uses in fields including dyes, agrochemicals, and medicines [5, 6]. Industrialists and researchers are keen to work on the heterocyclic containing compounds owing to their interesting chemistry features [7], attractive and tunable characteristics like drug effectiveness [8] and crop treatment [9]. Out of numerous potent heterocyclic compounds, one compound from this class is indole predominately characterized via a combination of a pyrrole ring with a benzene ring [10]. Molecular systems containing indole are frequently exploited in order for having potent anti-inflammatory [11], antimicrobial [12], antiviral [13], antitumor [14], and anticancer [15] characteristics/properties, including their usage as anti-corrosion material and in hygienic treatments [16]. When metals undergo deterioration owing to their chemical interactions with their adjacent environment, this phenomenon is referred to as corrosion [17, 18]. It is a determined and continuing issue that is often challenging to eliminate [19]. As a result, concentrating on prevention is typically more practical and successful than trying to eradicate everything. Reaching at and exploring cost and quality effective organic corrosion inhibitors applicable in numerous environmental conditions has been the subject of extensive investigation [20, 21]. Examples of substances that are frequently employed as inhibitors in acidic chemical environments include nitrogen-based compounds along with associated derivatives, sulfur-based substances, thioaldehydes, aldehydes, acetylenic substances, and different alkaloids like papaverine, strychnine, quinine, and nicotine [22]. Organic inhibitors typically composed of heteroatoms (non-carbon atoms) like nitrogen, oxygen, and sulfur, which possess higher electron density and basicity, making them active sites for adsorption onto metal surfaces. The effectiveness of these elements in inhibition generally increases in the order of $O < N < S < P$. The corrosion-reducing properties of organic compounds particularly those containing nitrogen, sulfur, and oxygen on steel have been extensively investigated [23]. Considering the wide spectrum of organic inhibitor types, dyes containing heteroatoms such as nitrogen, oxygen, and sulfur have shown considerable promise due to their strong interaction with metal surfaces via π-electron systems and lone-pair electrons [24]. Moreover, in case of heteroatoms containing compounds, there are numerous centers having high electronegativity and such centers/atoms are easily targeted by the metals those d-orbitals which are vacant. Structure of dyes have π-conjugated molecular backbones which are pretty effective in order to provide possibility of efficient processes on metal–solution interface such as electron donation process as well as electron back-donation process. These sorts of interactions enabled to form a smooth and stable adsorbed layer which is used as an effective protective barrier against corrosive species. In this context, indole-based dyes have emerged as potent corrosion inhibitors, owing to their unique molecular structure and electronic characteristics. D149, a commercially available indole dye primarily used in dye-sensitized solar cells (DSSCs), has recently been investigated for its corrosion inhibition properties [25]. By adding different substituents, indole structures may be modified to improve their electrical characteristics [26] and, as a result, their inhibitory efficacy. Prior to experimental confirmation, theoretical techniques specifically, the computational

models used to study quantum chemical and molecular dynamic principles represent an inexpensive yet precise means to assess the efficacy of a wide variety of inorganic molecules against corrosion prior to performing any related experimental work [27]. The electronic structures, including frontier orbitals and charge densities, will provide a greater understanding of how each inorganic molecule will interact with a metal surface. Furthermore, molecular dynamics simulations allow researchers to study the plasticity, orientation and attachment strength of the interfaces/bonds formed by investigated inhibitors and substrates. By applying quantum chemistry and molecular dynamics, researchers can simulate how an inhibitor will shield from corrosion, considering different environmental conditions through a simulated molecular interaction between inhibitor and substrate. This type of study will substantially decrease laboratory testing to identify the most efficient inhibitors against corrosion. Quantum chemistry and molecular modeling also reduce the cost, time, and material waste while developing inorganic corrosion prevention inhibitors. By using this method of computational screening on several potential inhibitors that employ a common theoretical basis, only the most viable inhibitors will be identified and tested in the laboratory. Consequently, the combination of quantum chemistry and molecular dynamic modeling facilitates the advancement of advanced materials for corrosion prevention with better performance characteristics than existing corrosion prevention materials [28]. Potent capabilities of the indole-based compounds/substances on Fe surfaces make them pretty suitable for wide range of applications [29–32]. For example, these compounds are used as cleaner in numerous industrial processing involving iron, as protector of carbon steel-based pipelines as a heat exchanger in petrochemical processing unit. The molecular environment, orbital energies (HOMO–LUMO), dipole moment, global hardness, and adsorption energies all of which are closely linked to the reactivity and intensity of inhibitor interaction with metal surfaces can be analyzed using these techniques. By utilizing this computational technique, researchers are enabled to reveal not only the electronic characteristics of compounds but also pretty helpful in providing knowledge about the inhibition potential of compounds on metal surfaces like iron surfaces. The characteristics of the compound known as dipole moment which is calculated by theoretical method assessed polarity of molecule of the compound and this information is further helpful in revealing the capability of the compound to align with the metal surfaces in case of external electric filed applied. In summary, computational/theoretical realm is pretty helpful in design of new and more effective corrosion inhibitors [33, 34]. The objective of this study is to use computational chemistry and molecular modeling to provide a theoretical framework for evaluating selected indole derivatives (see Fig. 1) as potential corrosion inhibitors for iron surfaces. Density functional theory was used to investigate electronic structure properties of the compounds with the aim of understanding how different electronic structural characteristics may affect corrosion inhibition ability through their reactivity with iron surfaces and their interaction of this type. Frontier molecular orbitals and charge distributions were assessed to determine the electron-donating ability (back-donating) of each molecule. Adsorption configurations and relative strengths of each of these interactions with the iron substrate were also researched via molecular simulation techniques. Using this combination of computational techniques,

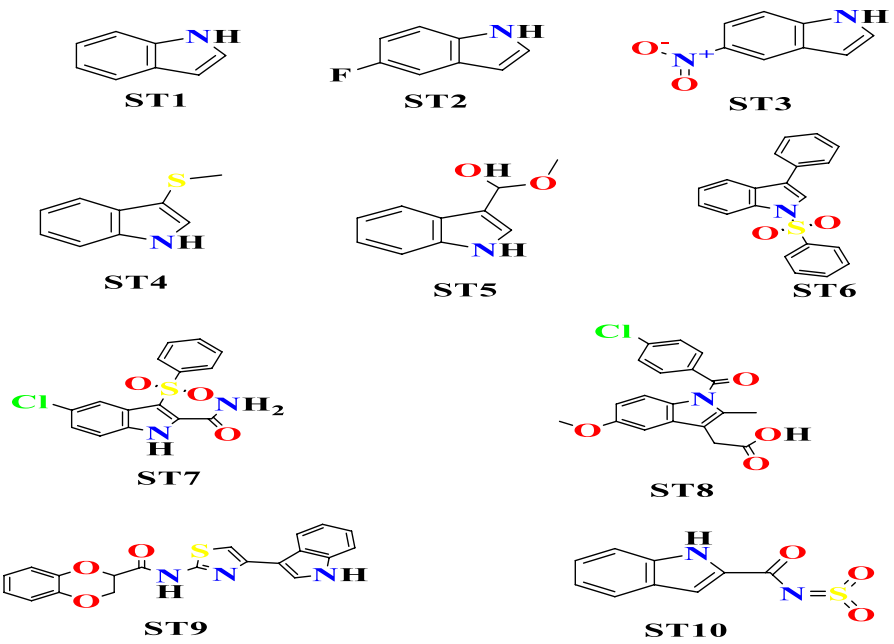


Fig. 1 2D Molecular structures for selected Indole derivatives **ST1–ST10**

relationships between electronic structural properties and their adsorption behavior can be established. These relationships provide an important foundation for understanding the detailed mechanism of inhibition at the molecular level is provided by how variations in the molecular structure of the indole derivatives can influence the affinity of the molecule for the surface of an iron substrate and how the thermodynamic and geometric parameters that affect corrosion inhibition performance can be systematically evaluated. These findings identify the essential features that contribute to the overall effectiveness ofcorrosion protection provided by different indole derivatives. Therefore, this study also has implications for providing a rational basis for selecting corrosion inhibitors based on their structural and electronic properties. Thus, this research has established a theoretical basis for designing advanced and more effective corrosion inhibitors.

Theoretical Study

Density Functional Theory Calculations

For generating the molecular structure geometries of substances **ST1–ST10**, the molecular visualization program GaussView 6.0. 16 was applied (Fig. 1). For optimization the structures at DFT/B3LYP/6–311++G(2d,p), the Gaussian 09, Revision D.01 algorithm was utilized [35]. GaussView 6.0. 16 [36] chemical structure visualization

software was applied to evaluate the E_{HOMO}, $E_{LUMO,}$ and molecular electrostatic potential (MEP) maps, UV spectroscopy.

Topological Analyses

The Electron Localization Function (ELF), analysis [37], non-covalent interactions (NCI), and reduced density gradient (RDG) analysis of **ST1–ST10** compounds were examined using Multiwfn 3.7 bin Win64 software [38]. In the theoretical framework for ELF study, the components that are utilized include the color-filled map, the plain *x* and *y* axes, and the input *z*-axis value of 0.2 Bohr units [39].

Monte Carlo Calculations

Monte Carlo (MC) simulations were performed using the Adsorption Locator module in the Materials Studio program. The COMPASSIII parametric force field was utilized in this study owing to its verified preference precision in the context of modeling adsorption processes, especially when it comes to systems containing metallic surfaces and organic corrosion inhibitors. The force field-based parameters guaranteed a realistic illustration of molecular interactions like van der Waals and electrostatic interactions for the aim of replicating adsorption events. To accurately represent the solid metal, the Fe (110) slab was constructed using 5 atomic layers that were subsequently expanded into a 9×9 supercell. During the simulations, the bottom atomic layers of the slab were kept fixed at their bulk crystallographic positions to represent the semi-infinite bulk metal, while the upper surface layers and the adsorbing molecules were allowed to fully relax. Each iteration used 60,000 steps of simulated annealing to efficiently find equilibrium states and investigate possible configurations. The Ewald summation method was used to evaluate the electrostatic interactions (ESI) to an accuracy/precision of 10^{-5} kcal mol^{-1} [40], providing the possibility for achieving optimal reliability regarding the capturing of long-range interactions. The simulations were conducted in two distinct environments: a dry environment (inhibitor in a vacuum) and an acidic environment. To simulate the acidic environment, the simulation box included 100 water molecules, the inhibitor molecule, four hydronium ions (H_3O^+), and two sulfate ions (SO_4^{2-}). This specific ionic ratio was strictly employed to guarantee overall charge neutrality within the simulation box (i.e., $4(+1) + 2(-2) = 0$). Periodic interactions were reduced by applying a 25 Å vacuum layer along the *C*-axis. The adsorption energy (E_{ads}) was calculated using the equations provided in the supplementary file, and the binding energy is defined strictly as the negative of the adsorption energy ($E_{binding} = -E_{ads}$).

Results and Discussion

Study of HOMO–LUMO energy profiling along with and other vital quantum chemical computations are frequently utilized to produce precise predictions about the efficacy of corrosion inhibition. Computational studies clearly show that the success

of an inhibitor will depend mainly on its capacity to transport electronic charge bidirectionally through the metal interface. Transfer of electrons from highest occupied states and to lowest unoccupied states facilitate stable interactions with surface atoms; consequently, these charge transfer processes support the solid adsorption of the inhibitor and creation of a complete protective layer. Thus, the magnitude of the interfacial adhesion will be critical in preventing corrosion [41].

One significant element that is impacted by the transfer of charge between atoms is the dipole moment. The system, which is made up of various atoms, is said to be polar. The electron affinities of the constituents determine the polarity of the interaction. It implies that a bond's degree of polarity controls how much its electron density fluctuates. The dipole moment is a defining characteristic of an ionic chemical connection [42]. At first, optimization of molecular structures of compounds **ST1–ST10** is done at DFT/B3LYP/6–311++G(2d,p) basis set (Fig. 2). The total dipole moment (μ_D) and its vector components (μ_x, μ_y, μ_z) provide insights into the molecular orientation and the ability of the inhibitor to displace water molecules from the metal surface. As shown in Table S1, the studied compounds exhibit a wide range of values, with **ST3** displaying the highest dipole moment (7.611 Debye), likely due to the strong electron-withdrawing nature of the nitro group. Conversely, **ST8** exhibits the lowest dipole moment among the investigated compounds at 1.883 Debye (Fig. 3).

Notably, **ST10** possesses a moderate and balanced dipole moment (3.943 Debye) compared to the more polar derivatives like **ST3** and **ST9**. From a

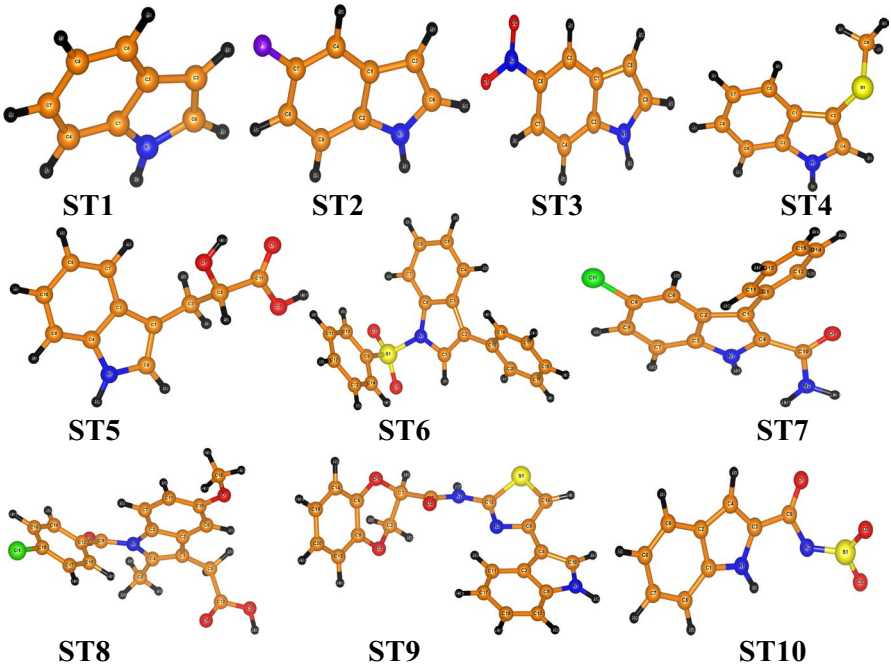


Fig. 2 Best optimize shape of **ST1–ST10** compounds

mechanistic standpoint, the moderate dipole moment of **ST10**, combined with its high global softness, suggests a more uniform electron density distribution. This allows **ST10** to effectively maintain a flat, parallel orientation on the iron surface, maximizing the contact area of its extended π-conjugation and indole nitrogen lone pairs with the Fe d-orbitals.

The superior inhibition efficiency of **ST10** suggests that molecular polarizability and a balanced dipole are better indicators of stable, long-term film formation. The low μ_z component in **ST10** further confirms its tendency to lie parallel to the Fe (110) plane, ensuring effective surface coverage and a more robust protective barrier against the acidic medium.

The frontier molecular orbital energies, specifically E_{HOMO} and E_{LUMO} (illustrated in Fig. 4), play a vital role in determining the reactivity of the inhibitor molecules. The E_{HOMO} is associated with the electron-donating ability of the molecule, where a higher (less negative) value indicates a greater tendency to donate electrons to the vacant d-orbitals of the iron surface. As shown in Table S1, **ST9** exhibits the highest E_{HOMO} at − 5.462 eV, followed closely by **ST5** at − 5.661 eV. Conversely, the E_{LUMO} indicates the molecule's ability to accept electrons from the metal surface (back-donation). Lower (more negative) E_{LUMO} values correspond to better electron-accepting capabilities. The lowest E_{LUMO} is observed for **ST10** (− 3.151 eV) and ST3 (− 2.447 eV), while **ST6** and **ST7** exhibit E_{LUMO} values of − 1.787 and − 1.799 eV, respectively.

The energy gap is a decisive indicator of a molecule's overall chemical reactivity and stability. A smaller energy gap implies lower excitation energy, facilitating easier electron transfer and stronger adsorption onto the metal surface. Based on the calculated data in Table S1 and the energy diagrams shown in Fig. 4, **ST10** possesses the narrowest energy gap (3.339 eV), making it the most highly reactive compound among those studied.

By evaluating the ΔE, the predicted order of corrosion inhibition potential for the investigated compounds is established as follows: **ST10** (3.339 eV) > **ST8** (3.842 eV) > **ST9** (4.040 eV) > **ST3** (4.101 eV) > **ST6** (4.238 eV) > **ST7** (4.317 eV) > **ST5** (4.943 eV) > **ST4** (5.076 eV) > **ST2** (5.138 eV) > **ST1** (5.183 eV). This trend clearly demonstrates that **ST10** has the most favorable electronic properties

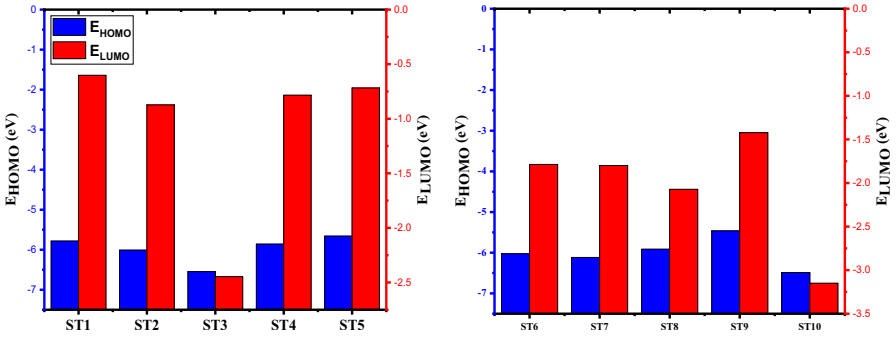


Fig. 3 Barnhart representations of energy HOMO, and LUMO

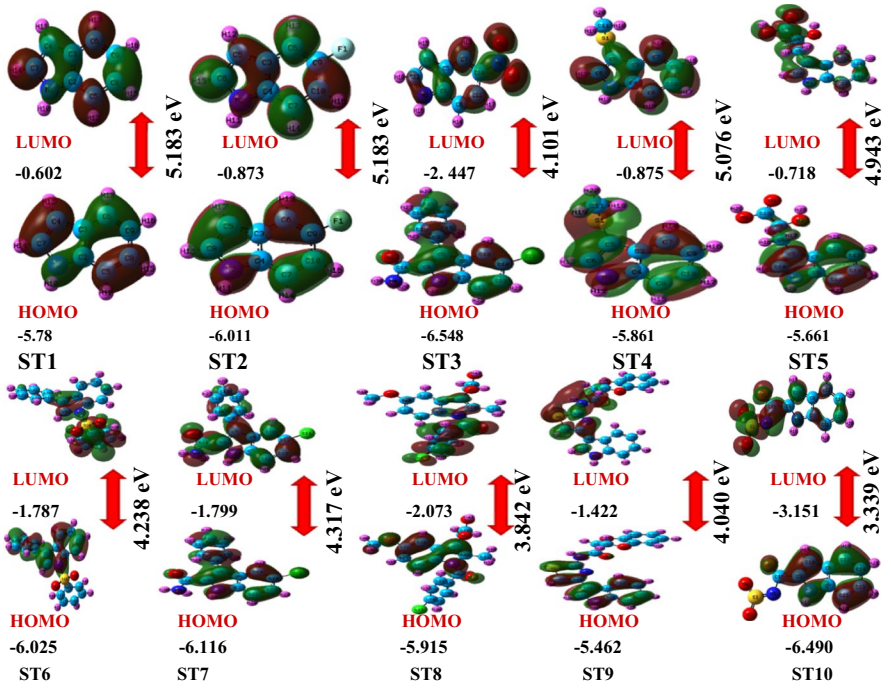


Fig. 4 HOMO, LUMO energy diagram for studied compounds

for effective interaction with the iron surface, while **ST1** shows the least theoretical reactivity.

All of the studied structures are characterized by electrophilicity index values > 1.5 eV, demonstrating their significant electrophilic nature (Table S1). To rigorously examine the charge transfer and adsorption behavior, we evaluated the fractional number of transferred electrons (ΔN) utilizing the established work function ($\Phi = 4.82$ eV) for the Fe metal surface (Φ is a work function) [43, 44]. The molecule-to-metal electron charge transfer was calculated using the formula $\Delta N = (\Phi - \chi)/(2\eta)$. While most compounds exhibited forward donation, the calculations revealed that ST10 possesses a slight negative charge transfer value (− 0.0002). This tiny electron transfer from the Fe surface to the molecule is a direct result of **ST10**'s electron-withdrawing group, which lowers the overall electron density on the molecule. Consequently, this leads to a favorable back-donation (− 0.417 eV) where electrons flow from the occupied states of the Fe metal back into the vacant orbitals of the inhibitor, thereby strengthening the adsorption.

Comparison of the MEP maps of **ST1–ST10** revealed influence variety chemical attached function groups. For **ST1–ST10**, the most noticeable electrophilic centers, almost blue areas (electron-deficient regions), and positive MEP were found to be the hydrogen (H) atoms joined to the nitrogen (N) atoms (Fig. 5) [41].

The electronic properties of the indole derivatives **ST1–ST10**, specifically the refractive index (n) and the dielectric constant (ϵ), are summarized in Table 1.

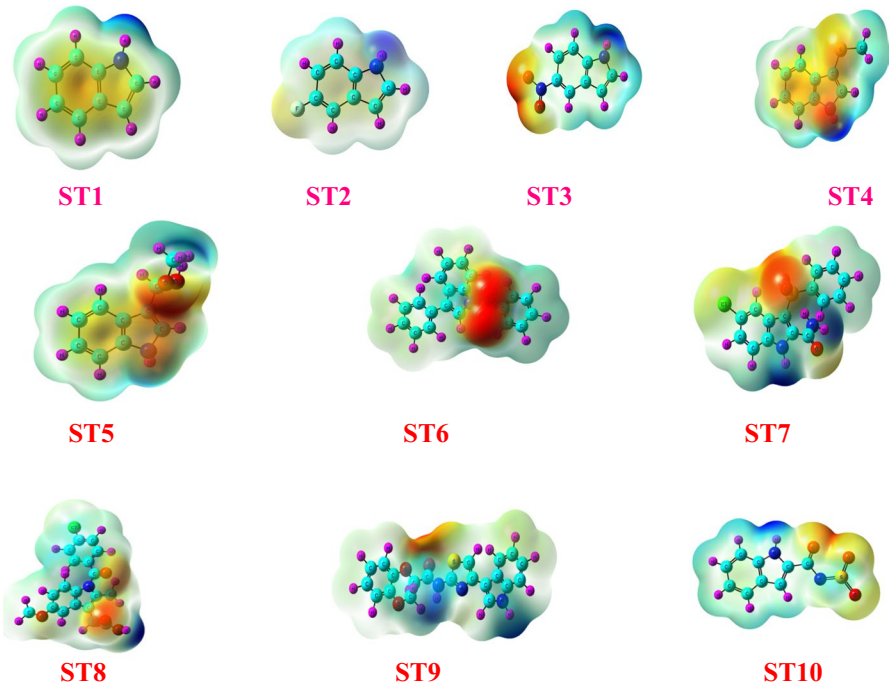


Fig. 5 ESP maps for studied compounds

Table 1 Computed: dielectric constant (ε), dielectric constant (ε): $\varepsilon = n^2$; refractive index (n), using Tripathy relation $n = n_o \times \left[1 + \frac{\alpha}{e^{\beta E_g}}\right]$, when n_0, α, and β are as 1.73, 1.9017, and 0.539 $(\text{eV})^{-1}$; and the Kumar relation method $n = 3.3668(E_d^g)^{-0.32234}$ [42, 45]

Compounds	Refractive index (n) [46, 47]		Dielectric constant (ε) [46, 48]	
	Kumar relation	Tripathy relation	Kumar relation	Tripathy relation
1ST	1.981	1.931	3.924	3.730
ST2	1.987	1.936	3.946	3.749
ST3	2.136	2.091	4.564	4.371
ST4	1.994	1.943	3.977	3.776
ST5	2.011	1.959	4.046	3.838
ST6	2.114	2.065	4.468	4.265
ST7	2.101	2.051	4.415	4.207
ST8	2.182	2.145	4.760	4.600
ST9	2.147	2.103	4.608	4.422
ST10	2.283	2.274	5.210	5.171

A clear inverse relationship is observed between the HOMO–LUMO energy gap and the refractive index across the series. **ST10**, which possesses the narrowest

energy gap (3.339 eV), exhibits the highest refractive index ($n \approx 2.28$) and dielectric constant ($\epsilon \approx 5.21$). In the context of corrosion inhibition, these values are indicative of high molecular polarizability. This suggests that the electron cloud of **ST10** is highly deformable, allowing it to easily adapt its electronic structure to form stable interactions with the Fe (110) surface, thereby enhancing its inhibitory performance.

To gain insights into the spatial distribution of electron density and identify potential reactive sites, the Electron Localization Function (ELF) was computed using the Multiwfn software [49]. The ELF is a topological descriptor normalized on a scale from 0 to 1, providing a clear distinction between highly localized and delocalized electron distributions. Specifically, Regions of Localized Electron density (RLE) such as covalent bonds and lone pairs exhibit high ELF values ranging from 0.5 to 1.0. In contrast, regions with ELF values less than 0.5 indicate delocalized electron density or electron depletion zones.

The computed ELF maps of the investigated indole derivatives effectively illustrate these distinct electronic properties. The carbon–carbon (C–C) linkages within the aromatic rings exhibit high ELF values in the internuclear regions, confirming a high degree of electron sharing and strong covalent bonding. Furthermore, the ELF maps reveal prominent regions of intense electron localization localized around the heteroatoms (oxygen, nitrogen, and sulfur). These specific high-density zones correspond to non-bonding lone-pair electrons. Identifying these highly localized lone pairs is vital from a mechanistic standpoint, as they serve as the primary nucleophilic centers responsible for donating electron density to the vacant d-orbitals of the metal surface, thereby facilitating strong coordinate bonding and effective corrosion inhibition (Fig. 6).

The Reduced Density Gradient (RDG) scatter plots of the investigated indole derivatives (Fig. 7) provide valuable insights into the nature of their intramolecular non-covalent interactions. By mapping the RDG against $sign(\lambda_2)\rho$, the plots for compounds **ST1–ST10** generally reveal prominent spikes in the positive region ($sign(\lambda_2)\rho > 0$), indicative of strong steric repulsion (ring strain), alongside features near zero ($sign(\lambda_2)\rho \approx 0$) that correspond to weak van der Waals (vdW) interactions. Notably, the derivatives **ST5–ST9** exhibit particularly distinct vdW interaction signatures. Furthermore, the RDG plots for **ST4, ST5, ST6, ST8, and ST9** display broad and pronounced spikes extending deep into the negative region ($sign(\lambda_2)\rho < 0$). This characteristic distribution confirms the presence of strong intramolecular attractive forces, such as hydrogen bonding or favorable electrostatic attractions, which significantly contribute to the structural and conformational stability of these molecules.

To spatially visualize these interactions, 3D Non-Covalent Interaction (NCI) isosurface plots were generated for all compounds (Fig. 8). The emergence of green-colored isosurfaces in these topological maps visually confirms the specific regions where weak van der Waals interactions and structural delocalization occur. For instance, prominent green isosurfaces are localized between the nitro group and adjacent C–H bonds in **ST3**, as well as between the hydroxyl and carbonyl functionalities in **ST5**. Similar stabilizing interaction zones are observed around the sulfonyl-containing functional groups in **ST6**, and specifically localized between the N=S

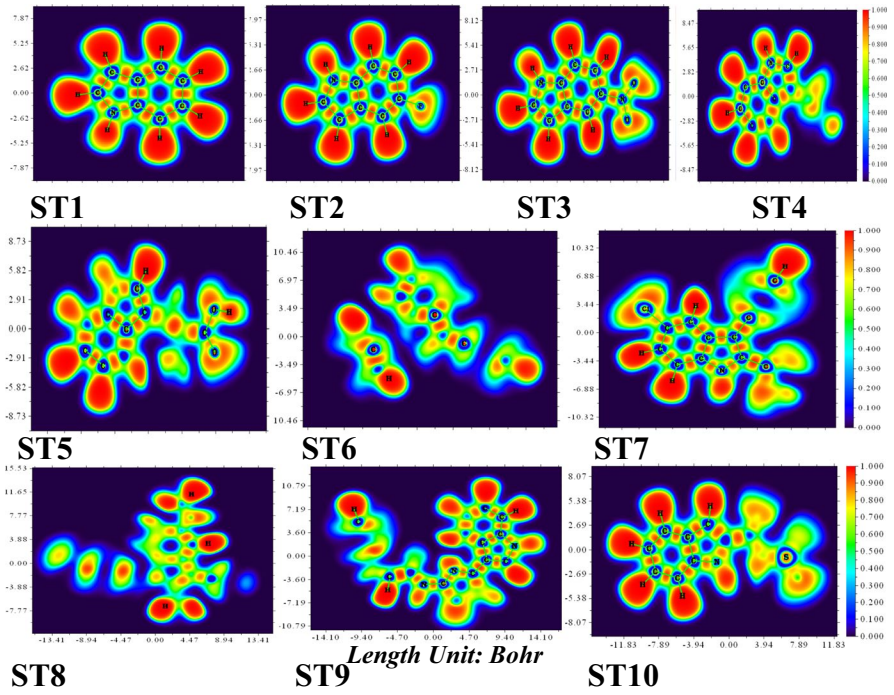


Fig. 6 ELF maps for studied compounds

bond, oxygen atoms, and the carbonyl group in **ST10**. These intramolecular non-covalent interactions play a crucial role in restricting molecular rotation and enforcing coplanarity, which ultimately enhances the ability of the inhibitors to maintain a flat, parallel adsorption posture on the metal surface.

To complement the macroscopic work function analysis, the specific donor–acceptor interaction modes were further evaluated at the microscopic level using localized energy differences (ΔE_1 and ΔE_2). We explicitly acknowledge that macroscopic bulk metals are described by a continuous band structure and do not possess discrete HOMO/LUMO levels. Therefore, the ΔE_1 and ΔE_2 descriptors presented here are calculated using the discrete ionization energy and electron affinity of a single, isolated Fe atom. This approach serves strictly as a localized "single-adatom approximation" to model the interaction between the inhibitor molecules and a single, discrete active site on the metal surface.

The energy separation between these respective electronic states provides insight into the highly localized charge transfer through the interface. ΔE_2 represents the energy barrier for forward electron donation from the inhibitor's HOMO to the vacant d-orbitals of the Fe atom, while ΔE_1 represents the energy barrier for back-donation from the occupied states of the Fe atom to the inhibitor's LUMO. A smaller energy gap indicates a more energetically favorable interaction.

The outcomes attained here reveal that for compounds **ST1**, **ST2**, and **ST4–ST9**, the value of ΔE_2 is smaller than ΔE_1 (Table 2). This indicates that at localized active

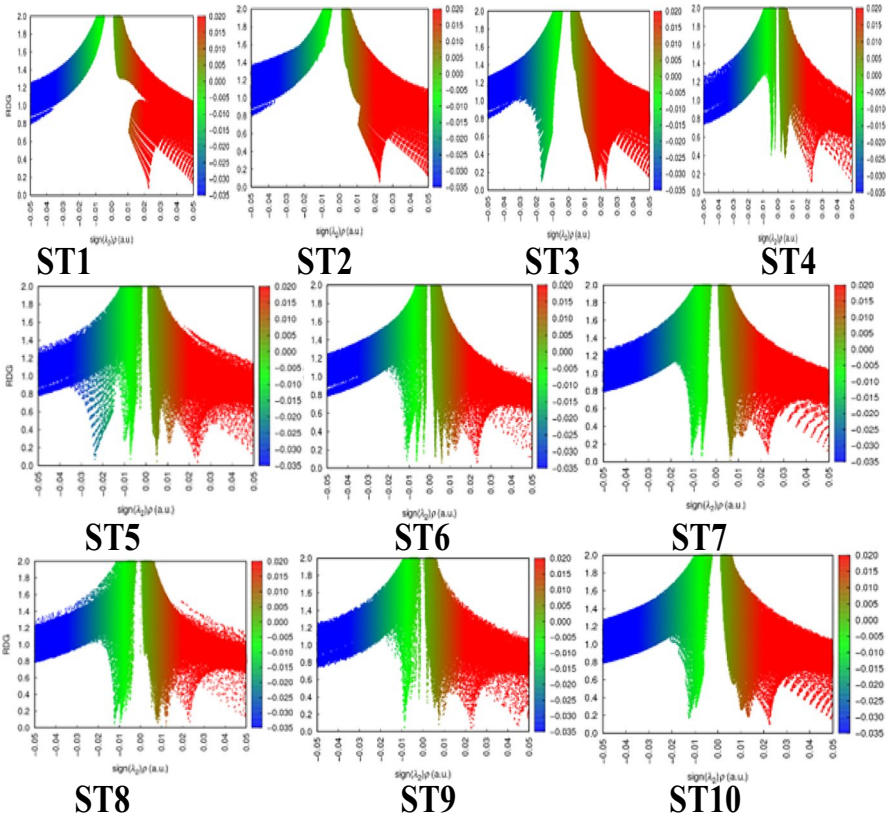


Fig. 7 RDG scatter for studied compounds

sites, the investigated inhibitors predominantly act as electron donors, easily providing electrons to the vacant d-orbitals of the Fe atom rather than accepting them. Conversely, for compounds **ST3** and **ST10**, $\Delta E_1 < \Delta E_2$. This denotes that localized back-donation from the Fe atom to the empty LUMO of these specific inhibitory molecules is the energetically favored process, largely due to the presence of electron-withdrawing substituents. Ultimately, the synergistic combination of these localized forward and back-donation interactions determines the adsorption strength and effectiveness of the inhibitor.

NBO Analyses

To predicate and assess bonding and antibonding orbitals, NBO were used to analyze the molecules **ST1–ST10** under discussion. NBO analysis provides additional insight into how electronic interactions shape the behavior of a specific system. According to NBO analysis, one of the main differences between Lewis type localized bonds and non-Lewis delocalized orbitals is that Lewis type localized bonds are

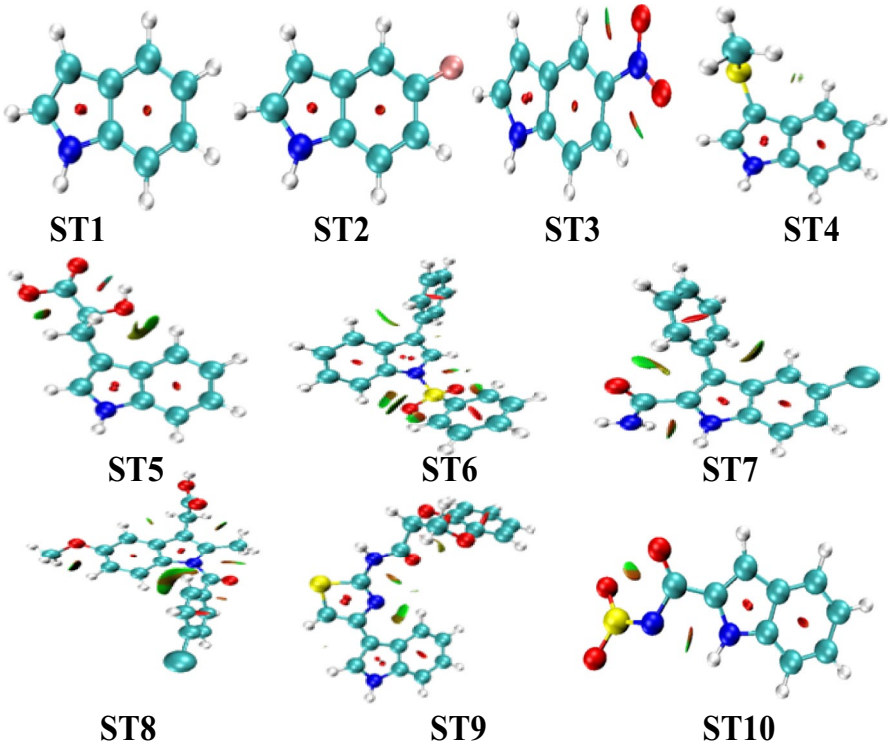


Fig. 8 NCI plots for the examined compounds

Table 2 Energy gaps between the inhibitory molecules and Fe metal surface

Fe									
ΔE_1									
ST1	ST2	ST3	ST4	ST5	ST6	ST7	ST8	ST9	ST10
7.3	7.029	5.455	7.117	7.184	6.115	6.103	5.829	6.48	4.751
ΔE_2									
5.634	5.86	6.397	5.71	5.51	5.874	5.965	5.764	5.311	6.339

All values are in eV

localized, while non-Lewis type delocalized orbitals contribute to a network of electron density redistribution throughout the molecule. Both bonding and antibonding orbitals in the NBO analysis can be used to explain why there are regions within the molecule that are highly populated with electron density and regions of very little or no electron density. This understanding creates the ability to predict how electron density is spread throughout the molecule and allows for visualization of potential pathways for intramolecular charge delocalization to increase the electronic stability of the molecule. Donor/acceptor interactions were identified in the NBO analysis

as being key to understanding how intermolecular charge transfer occurs, as well as elucidating the extent of electron donation and back-donation between the two interacting fragments. Therefore, NBO analysis provides insight into the nature and extent of electronic interaction in a molecular framework for achieving resonance stabilization within that specific molecular framework. Thus, NBO provides a comprehensive view of the electronic properties that contribute to the stability and reactivity of a given molecule. For each predicate donor NBO (i), acceptor NBO (j) value, and $E^{(2)}$ denoted with electron delocalization between the donor and acceptor, the second order energy predicts the stabilization energy, which indicates the intensity of the delocalization interactions [50, 51].

Larger $E^{(2)}$ values signify more robust interactions between electron-deficient and electron-rich molecules. Although all studied compounds show nine different electronic transitions ($\pi \rightarrow \pi^*$, $\pi^* \rightarrow \pi^*$, $\sigma \rightarrow \sigma^*$, $LP \rightarrow \sigma^*$, $LP \rightarrow \pi^*$, $\pi^* \rightarrow \sigma^*$, $\pi^* \rightarrow \sigma$, $\pi \rightarrow LP$, and $\sigma \rightarrow \pi$ *), the most significant interactions involve π-electron movement ($\pi \rightarrow \pi^*$, $\pi^* \rightarrow \pi^*$, and $\sigma \rightarrow \sigma^*$) and then lone-pair donation to antibonding π* orbitals ($LP \rightarrow \pi^*$) (Table S2). According of this, the stabilization energy ($E^{(2)}$ kcal/mol) interaction between a donor NBO (e.g., σ, π, lone pair) and an acceptor NBO (e.g., σ*, π*, empty orbital), the value of $\sigma \rightarrow \sigma^*$ larger than bonding to antibonding $\pi \rightarrow \pi^*$.

The Fukui function (f_k) is an excellent tool for identifying reactive sites on inhibitor molecules. Analyzing the Fukui function helps to elucidate the mechanism behind the corrosion inhibiting action of these molecules by indicating which parts of the molecule are most likely to participate in electron transfer reactions. Regions with a higher negative Fukui function (f_k^-) value show a higher level of effectiveness in donating electrons to the positively charged metal surface because effective potential corrosion inhibitors play the effective role of electron donors. This could aid the formation of a protective layer that stops corrosion. The condensed f_k is a useful indicator of a molecule's inherent nucleophilicity, whereas nucleophilic sites have a negative value denoted by f_k^-, atoms with a positive f_k^+ are classified as electrophilic indicates f_k^+. The highest values of f_k^- were revealed for C4, followed by H11, in **ST1**; C9 in **ST2**; C5 in ST**3**; and **S1** in **ST4;** C5, C10 in **ST5;** C1 in **ST6**; C1 in **ST7**; O2, C12 in **ST8**; S1 in **ST9**; and C10 in **ST10** (Fig. 9).

Monte Carlo (MC) Simulations

As shown in Table 5, the total, adsorption, and binding energies are significantly higher in the acidic environment (~ − 2700 kcal/mol) compared to the dry environment. This difference is physically consistent with the explicit solvent model, where the adsorption energy reflects the stabilization of the entire solvent-ion-inhibitor network on the surface. Notably, the adsorption energy values in the acidic medium are orders of magnitude larger than those in the dry environment, indicating a much more complex and energetic interaction between the inhibitor, the corrosive ions, and the metal slab.

The significant increase in E_{ads} is primarily driven by the explicit inclusion of hydronium (H_3O^+) and sulfate (SO_4^{2-}) ions, which exhibit high affinity for the Fe

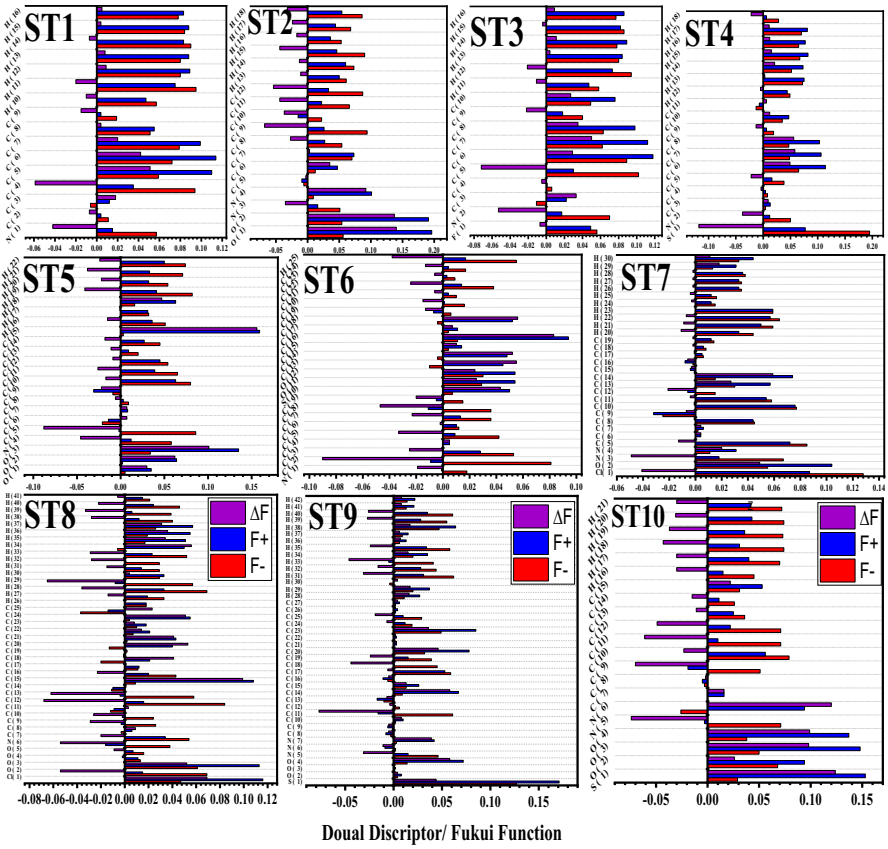


Fig. 9 Fukui functions for the **ST1–ST10**

(110) surface. As detailed in the specific components of the adsorption energy (Table 3), the individual contribution of (SO_4^{2-}) ions (ranging from − 553 to − 617 kcal/mol) and H_3O^+ ions (ranging from − 131 to − 150 kcal/mol) significantly lowers the total energy of the system. This suggests that the inhibitor does not adsorb in isolation but rather within a synergistic ionic layer where sulfate ions act as a bridge between the metal and the organic molecule, while hydronium ions facilitate a dense hydrogen-bonding network (Figs. 10, 11).

Although indole derivatives may protonate in bulk solution, they were modeled in their neutral molecular form to simulate direct coordination with the Fe surface via nitrogen lone pairs and the pi-electron system. The presence of explicit hydronium and sulfate ions allows for a realistic assessment of how these neutral inhibitors compete with solvent species and interact within a dense hydrogen-bonding matrix to anchor a protective layer to the metal surface.

Table 3 Adsorption energy (kcal/mol) calculated using the MC simulation of the studied compounds on the Fe (110) surface, (dry environment) (Acidic environment)

Compound	Total energy	Adsorption energy	Rigid adsorption	Deformation energy	dE_{ad}/dN_i	Binding energy
(Dry environment)						
ST1	80.115	− 71.383	− 71.945	0.562	− 71.383	71.383
ST2	70.723	− 74.562	− 75.155	0.593	− 74.562	74.562
ST3	85.054	− 83.911	− 84.369	0.458	− 83.911	83.911
ST4	54.269	− 96.161	− 97.019	0.858	− 96.161	96.161
ST5	48.718	− 110.794	− 115.198	4.404	− 110.794	110.794
ST6	141.168	− 166.575	− 183.731	17.155	− 166.575	166.575
ST7	117.309	− 135.979	− 139.750	3.771	− 135.979	135.979
ST8	− 54.695	− 171.857	− 189.936	18.079	− 171.857	171.857
ST9	35.897	− 117.891	− 118.799	0.908	− 117.891	117.891
ST10	− 5.748	− 174.634	− 176.838	2.205	− 174.634	174.634

					H_2O	H_3O^+	SO_4	
Acidic environment								
ST1	− 2750.53	− 2750.53	− 2850.00	99.46	− 13.44	− 131.49	− 617.37	2750.53
ST2	− 2760.97	− 2760.97	− 2861.06	100.09	− 14.27	− 144.41	− 584.35	2760.97
ST3	− 2733.23	− 2733.23	− 2842.00	108.78	− 19.40	− 144.12	− 578.49	2733.23
ST4	− 2739.04	− 2739.04	− 2844.09	105.05	− 14.30	− 147.21	− 577.10	2739.04
ST5	− 2714.23	− 2714.23	− 2817.12	102.89	− 13.66	− 146.92	− 582.21	2714.23
ST6	− 2675.96	− 2675.96	− 2783.23	107.27	− 15.31	− 140.33	− 594.79	2675.96
ST7	− 2705.30	− 2705.30	− 2813.07	107.77	− 14.58	− 142.81	− 553.66	2705.30
ST8	− 2671.76	− 2671.76	− 2782.03	110.28	− 15.35	− 150.58	− 571.44	2671.76
ST9	− 2695.84	− 2695.84	− 2802.89	107.06	− 13.85	− 142.37	− 566.10	2695.84
ST10	− 2783.81	− 2783.81	− 2845.73	101.91	− 16.05	− 141.03	− 604.74	2783.81

Conclusions

This in silico study employed a multiscale theoretical approach, including DFT calculations, topological analyses (NBO, RDG/NCI, Fukui functions), and Monte Carlo (MC) simulations to investigate the predicted corrosion inhibition performance of ten indole derivatives (**ST1-ST10**) on Fe surfaces. The integration of quantum chemical descriptors with non-covalent interaction visualization and adsorption simulations provided deep insights into the theoretical electronic characteristics, reactivity, and surface interactions of the inhibitors. The computational results suggest that high inhibitory effectiveness is likely driven by a combination of electron-rich regions, narrow HOMO–LUMO gaps, and strong adsorption affinities. While RDG and NCI investigations verified the theoretical existence of stabilizing non-covalent contacts, frontier molecular orbital theory and calculated adsorption energies indicated a predisposition toward spontaneous and directed charge transfer.

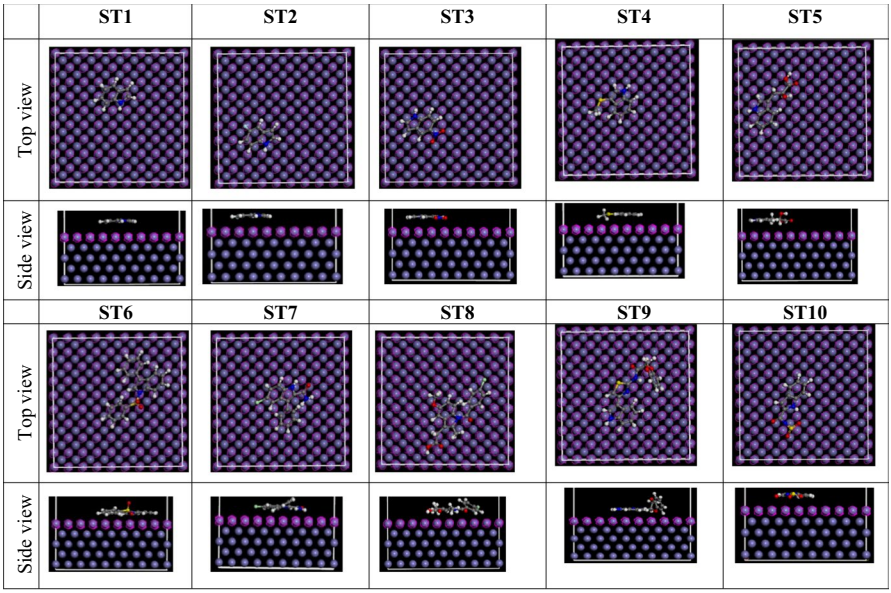


Fig. 10 Lowest energy and most energetically favorable adsorption geometries of the investigated compounds on the Fe(110) surface were identified through Monte Carlo-based simulations. (Dry environment)

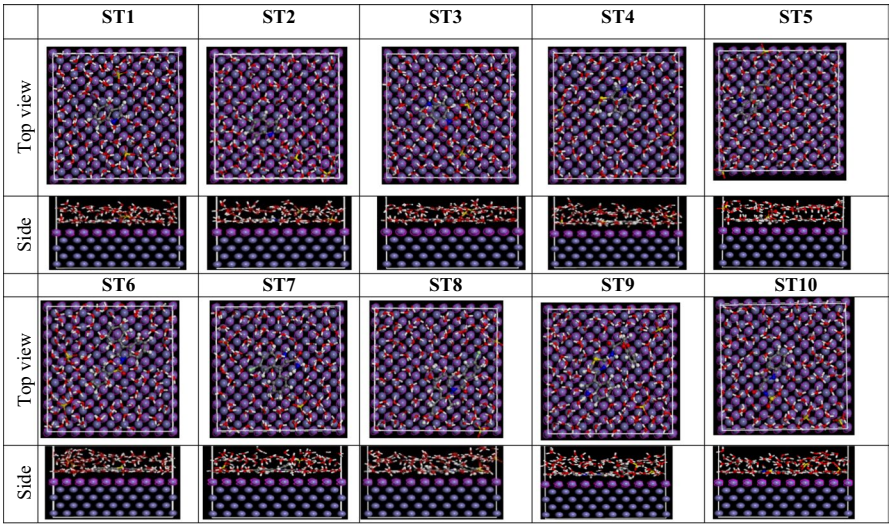


Fig. 11 Monte Carlo-based modeling identified the most favorable low-energy adsorption states of the studied molecules on the Fe (110) plane. (Acidic environment)

Among the investigated compounds, **ST10** demonstrated the highest predicted inhibitory potential due to its superior simulated adsorption behavior, strong electrophilicity, and narrow energy gap (3.339 eV). Additionally, **ST4**, **ST5**, and **ST9** showed electronic properties and binding affinities highly conducive to theoretically effective corrosion protection. These findings highlight the significance of structural tuning in the development of high-performance inhibitors.

However, it must be emphasized that these findings represent computational predictions rather than empirical proof of macroscopic performance. The actual corrosion inhibition efficiencies of these indole-based compounds remain pending rigorous experimental validation, such as electrochemical impedance spectroscopy and weight-loss measurements. To further bridge the gap between classical and quantum mechanical perspectives, future studies will focus on a direct quantitative comparison between DFT-derived chemisorption energies and Monte Carlo-based statistical adsorption trends to better refine multiscale corrosion modeling. These results open the door for the necessary experimental testing and potential industrial application of indole-based environment friendly inhibitors.

Supplementary Information The online version contains supplementary material available at https://doi.org/10.1007/s11085-026-10399-x.

Acknowledgements The authors would like to acknowledge the Department of Physics, University of Sargodha, for the support in the completion of this work.

Authors Contributions Authors contributions: Rebaz Obaid Kareem: Literature survey, writing draft. Kareem Jumaah Al-Salihi: performed DFT calculations and edit draft. Rebaz Anwar Omer: DFT calculations, supervison, methodology. Yousif Hussein Azeez: DFT part write up, review writing. Lana Omer Ahmed: Introduction writing, monte carlo simulations, editing draft. Muhammad Ashfaq: Formal analysis, administration, methadology, writing and review writing. Senem Akkoc: investigation, data curation, review writing. Aseel Smerat: Review writing, investigation. Mehran Feizi-Dehnayebi: investigation, writing, review writing, resources.

Funding Open access funding provided by the Scientific and Technological Research Council of Türkiye (TÜBİTAK).

Data Availability No datasets were generated or analyzed during the current study.

Declarations

Competing interest The authors declare no competing interests.

Ethics Approval This study did not involve humans, animals, or any ethical approvals.

Open Access This article is licensed under a Creative Commons Attribution 4.0 International License, which permits use, sharing, adaptation, distribution and reproduction in any medium or format, as long as you give appropriate credit to the original author(s) and the source, provide a link to the Creative Commons licence, and indicate if changes were made. The images or other third party material in this article are included in the article's Creative Commons licence, unless indicated otherwise in a credit line to the material. If material is not included in the article's Creative Commons licence and your intended use is not permitted by statutory regulation or exceeds the permitted use, you will need to obtain permission directly from the copyright holder. To view a copy of this licence, visit http://creativecommons.org/licenses/by/4.0/.

References

1. J. Saranya, M. Sowmiya, P. Sounthari, K. Parameswari, S. Chitra, and K. Senthilkumar, *Journal of Molecular Liquids* **216**, 42 (2016). https://doi.org/10.1016/j.molliq.2015.12.096.
2. C. P. Frizzo and M. A. P. Martins, *Structural Chemistry* **23**, 375 (2012). https://doi.org/10.1007/s11224-011-9883-z.
3. A. J. Lockley, A. C. Marr, G. C. Saunders, and H. P. Thomas, *The Journal of Fluorine Chemistry* **220**, 1 (2019). https://doi.org/10.1016/j.jfluchem.2019.01.006.
4. M. M. Khan and A. U. Malik, *Journal of Inorganic and Nuclear Chemistry* **35**, 247 (1973). https://doi.org/10.1016/0022-1902(73)80631-1.
5. R. Vicente, *Organic & Biomolecular Chemistry* **9**, 6469 (2011). https://doi.org/10.1039/C1OB05750B.
6. L. Zhou, P. Jing, W. Deng, S. Guo, Y. Liang, and Y. Yang, *Organic Chemistry Frontiers* **12**, 1122 (2025). https://doi.org/10.1039/D4QO02024C.
7. R. Kumar Maurya, A. Dey, V. Kumara, and M. Khatravath, *Asian Journal of Organic Chemistry* **13**, e202400259 (2024). https://doi.org/10.1002/ajoc.202400259.
8. M. Shokoohian, N. Hazeri, M. T. Maghsoodlou, and M. Lashkari, *Polycyclic Aromatic Compounds* **42**, 1 (2022). https://doi.org/10.1080/10406638.2020.1712439.
9. G. K. Sims, *Soil Biology & Biochemistry* **38**, 2478 (2006). https://doi.org/10.1016/j.soilbio.2006.01.006.
10. M. Düdükcü, B. Yazici, and M. Erbil, *Materials Chemistry and Physics* **87**, 138 (2004). https://doi.org/10.1016/j.matchemphys.2004.05.043.
11. M. Sayed, A.M. Kamal El-Dean, M. Ahmed, and R. Hassanien, *Synthetic Communications* **48**, 413 (2018). https://doi.org/10.1080/00397911.2017.1403627.
12. M. Giampieri, A. Balbi, M. Mazzei, P. La Colla, C. Ibba, and R. Loddo, *Antiviral Research* **83**, 179 (2009). https://doi.org/10.1016/j.antiviral.2009.05.001.
13. A.-R. Farghaly, *ARKIVOC* **11**, 177 (2010).
14. B. Prakash, A. Amuthavalli, D. Edison, M. S. Sivaramkumar, and R. Velmurugan, *Medicinal Chemistry Research* **27**, 321 (2018). https://doi.org/10.1007/s00044-017-2065-9.
15. A. Miralrio, and A. Espinoza Vázquez, *Processes* **8**, 942 (2020). https://doi.org/10.3390/pr8080942.
16. O. K. Abiola, N. C. Oforka, E. E. Ebenso, and N. M. Nwinuka, *Anti-Corrosion Methods and Materials* **54**, 219 (2007). https://doi.org/10.1108/00035590710762357.
17. R. Kocich, L. Kunčická, M. Benč, A. Weiser, and G. Németh, *International Journal of Biosciences* **10** (2024). https://doi.org/10.36922/ijb.1416.
18. M. Zhang, J. Wang, L. Peng, W. Yang, T. Zhao, B. Chen, Z. Zhao, and N. Dang, *Progress in Organic Coatings* **213**, 109956 (2026). https://doi.org/10.1016/j.porgcoat.2026.109956.
19. M. Bouklah, B. Hammouti, M. Benkaddour, and T. Benhadda, *Journal of Applied Electrochemistry* **35** 1095 (2005). https://doi.org/10.1007/s10800-005-9004-z.
20. H. Safa subhe, A.H.A.j. Haydar, and M.S.S. Ekbal, *Journal Computational Analysis and Applications* **33**, 1318 (2024).
21. A. Al-Amiery, W.N.R. Wan Isahak, and W.K. Al-Azzawi, *Ain Shams Engineering Journal* **15**, 102672 (2024). https://doi.org/10.1016/j.asej.2024.102672.
22. A. S. Fouda, A. A. Al-Sarawy, and E. E. El-Katori, *Desalination* **201**, 1 (2006). https://doi.org/10.1016/j.desal.2006.03.519.
23. A. Fiala, A. Chibani, A. Darchen, A. Boulkamh, and K. Djebbar, *Applied Surface Science* **253**, 9347 (2007). https://doi.org/10.1016/j.apsusc.2007.05.066.
24. M. Behpour, S. M. Ghoreishi, N. Mohammadi, N. Soltani, and M. Salavati-Niasari, Investigation of some Schiff base compounds containing disulfide bond as HCl corrosion inhibitors for mild steel. *Corrosion Science* **52**, 4046 (2010). https://doi.org/10.1016/j.corsci.2010.08.020.
25. J. Gong, K. Sumathy, Q. Qiao, and Z. Zhou, *Renewable and Sustainable Energy Review* **68**, 234 (2017). https://doi.org/10.1016/j.rser.2016.09.097.
26. Y. Gao, Z. Liu, S. Wang, A. Zhou, X. Lv, and X. Yue, *Science of the Total Environment* **951**, 175599 (2024). https://doi.org/10.1016/j.scitotenv.2024.175599.
27. C. Wang, L. Zhang, C. Chen, K. Dou, J. Zhang, C. Li, M. Gozin, W. Zhao, C. He, and S. Pang, *Journal of Materials Chemistry A* **13**, 26244 (2025). https://doi.org/10.1039/D5TA00267B.
28. X. Xie, K. Lin, Q. Gao, M. Jiang, and Y. Zhou, *International Journal of Food Microbiology* **445**, 111472 (2026). https://doi.org/10.1016/j.ijfoodmicro.2025.111472.
29. E. E. Salama, S. Alrashdi, A. T. A. Boraei, S. Eid, I. Gomaa, E. S. Gad, A. A. Elhenawy, and H. Nady, *Molecules* **30**, 1235 (2025). https://doi.org/10.3390/molecules30061235.

30. T. K. Sarkar, M. Yadav, and I. B. Obot, *Chemical Engineering Journal* **431**, 133481 (2022). https://doi.org/10.1016/j.cej.2021.133481.
31. B. T. D. My, D. Tuan, and D. Q. Huong, *Journal of Molecular Structure* **1296**, 136905 (2024). https://doi.org/10.1016/j.molstruc.2023.136905.
32. J. Li, L. Li, j. Fei, P. Zhao, J. Zhao, and Y. Xie, *Microchemical Journal* **200**, 110426 (2024). https://doi.org/10.1016/j.microc.2024.110426.
33. H. H. Rasul, D. M. Mamad, Y. H. Azeez, R. A. Omer, and K. A. Omer, *Computational and Theoretical Chemistry* **1225**, 114177 (2023). https://doi.org/10.1016/j.comptc.2023.114177.
34. A. I. Ikeuba, B. I. Ita, C. P. Okonkwo, P. E. Ekuri, H. O. Edet, J. Amajama, and P. C. Iwuji, *Discover Chemical Engineering* **4**, 28 (2024). https://doi.org/10.1007/s43938-024-00065-6.
35. M.J. Frisch, G.W. Trucks, H.B. Schlegel, G.E. Scuseria, M.A. Robb, J.R. Cheeseman, G. Scalmani, V. Barone, G.A. Petersson, H. Nakatsuji, X. Li, M. Caricato, A.V. Marenich, J. Bloino, B.G. Janesko, R. Gomperts, B. Mennucci, H.P. Hratchian, J.V. Ortiz, A.F. Izmaylov, J.L. Sonnenberg, Williams, F. Ding, F. Lipparini, F. Egidi, J. Goings, B. Peng, A. Petrone, T. Henderson, D. Ranasinghe, V.G. Zakrzewski, J. Gao, N. Rega, G. Zheng, W. Liang, M. Hada, M. Ehara, K. Toyota, R. Fukuda, J. Hasegawa, M. Ishida, T. Nakajima, Y. Honda, O. Kitao, H. Nakai, T. Vreven, K. Throssell, J.A. Montgomery Jr., J.E. Peralta, F. Ogliaro, M.J. Bearpark, J.J. Heyd, E.N. Brothers, K.N. Kudin, V.N. Staroverov, T.A. Keith, R. Kobayashi, J. Normand, K. Raghavachari, A.P. Rendell, J.C. Burant, S.S. Iyengar, J. Tomasi, M. Cossi, J.M. Millam, M. Klene, C. Adamo, R. Cammi, J.W. Ochterski, R.L. Martin, K. Morokuma, O. Farkas, J.B. Foresman, and D.J. Fox, Gaussian 09, Revision d. 01, Gaussian, Inc., Wallingford, CT, 2009.
36. R. Dennington, T.A. Keith, and J.M. Millam, GaussView 6.0. 16, Semichem Inc.: Shawnee Mission, KS, USA, 2016.
37. A. D. Becke and K. E. Edgecombe, *Journal of Chemical Physics* **92**, 5397 (1990). https://doi.org/10.1063/1.458517.
38. T. Lu and F. Chen, *Journal of Computational Chemistry* **33**, 580 (2012). https://doi.org/10.1002/jcc.22885.
39. E. R. Johnson, S. Keinan, P. Mori-Sánchez, J. Contreras-García, A. J. Cohen, and W. Yang, *Journal of the American Chemical Society* **132**, 6498 (2010). https://doi.org/10.1021/ja100936w.
40. Y. Hussein Azeez, R. Obaid Kareem, L. Omer Ahmed, R. Anwar Omer, K. Ahmed Othman, and D.A. Safin, *Computational and Theoretical Chemistry* **1240**, 114803 (2024). https://doi.org/10.1016/j.comptc.2024.114803.
41. R. A. Omer, Y. H. Azeez, R. O. Kareem, L. O. Ahmed, and D. A. Safin, *Journal of Fluorescence* (2025). https://doi.org/10.1007/s10895-024-04117-6.
42. S. Das, P. Ranjan, and T. Chakraborty, *Journal of Mathematical Chemistry* **62**, 2827 (2024). https://doi.org/10.1007/s10910-023-01569-2.
43. H. Bourzi, R. Oukhrib, B. El Ibrahimi, H. Abou Oualid, Y. Abdellaoui, B. Balkard, S. El Issami, M. Hilali, L. Bazzi, and C. Len, *Sustainability* **12**, 3304 (2020). https://doi.org/10.3390/su12083304.
44. H. L. Skriver and N. M. Rosengaard, *Physical Review B* **46**, 7157 (1992). https://doi.org/10.1103/PhysRevB.46.7157.
45. F. Naccarato, F. Ricci, J. Suntivich, G. Hautier, L. Wirtz, and G.-M. Rignanese, *Physical Review Materials* **3**, 044602 (2019). https://doi.org/10.1103/PhysRevMaterials.3.044602.
46. R.R. Reddy, K. Rama Gopal, K. Narasimhulu, L.S.S. Reddy, K.R. Kumar, C.V.K. Reddy, and S.N. Ahmed, *Optical Materials* **31**, 209 (2008). https://doi.org/10.1016/j.optmat.2008.03.010.
47. R. R. Reddy, K. R. Gopal, K. Narasimhulu, L. S. S. Reddy, K. R. Kumar, G. Balakrishnaiah, and M. R. Kumar, *Journal of Alloys and Compounds* **473**, 28 (2009). https://doi.org/10.1016/j.jallcom.2008.06.037.
48. R. O. Kareem, R. A. Omer, Y. H. Azeez, L. O. Ahmed, and O. A. Hamad, *Computational and Theoretical Chemistry* **1241**, 2024 114938. https://doi.org/10.1016/j.comptc.2024.114938.
49. K. M. Ahmed, R. A. Muhammed, R. A. Omar, Y. H. Azeez, R. O. Kareem, R. F. Rashid, E. V. Panova, and D. A. Safin, *Journal of Molecular Structure* **1338**, 142235 (2025). https://doi.org/10.1016/j.molstruc.2025.142235.
50. R. A. Omer, Y. H. Azeez, R. O. Kareem, L. O. Ahmed, and D. A. Safin, *Journal of Molecular Modeling* **30**, 288 (2024). https://doi.org/10.1007/s00894-024-06090-0.
51. F. Weinhold, C. R. Landis, and E. D. Glendening, *International Reviews in Physical Chemistry* **35**, 399 (2016). https://doi.org/10.1080/0144235X.2016.1192262.

Publisher's Note Springer Nature remains neutral with regard to jurisdictional claims in published maps and institutional affiliations.

Authors and Affiliations

Rebaz Obaid Kareem[1] · Kareem Jumaah Al-Salihi[2] · Rebaz Anwar Omer[3] · Yousif Hussein Azeez[1] · Lana Omer Ahmed[4] · Muhammad Ashfaq[5] · Senem Akkoc[6,7] · Aseel Smerat[8,9] · Mehran Feizi-Dehnayebi[6]

✉ Yousif Hussein Azeez
yousif.husain@uoh.edu.iq

✉ Muhammad Ashfaq
ashfaq.muhammad@uos.edu.pk

✉ Senem Akkoc
senemakkoc@sdu.edu.tr

Mehran Feizi-Dehnayebi
mehrandehnayebi@sdu.edu.tr

[1] Physics Department, College of Science, University of Halabja, 46018 Halabja, Iraq

[2] Department of Chemistry, College of Science, University of Sulaimani, Sulaymaniyah 46001, Iraq

[3] Department of Chemistry, Faculty of Sciences and Health, Koya University, Koya 44023, Kurdistan Region – F.R., Iraq

[4] Department of Physics, Faculty of Sciences and Health, Koya University, Koya 44023, Kurdistan Region – F.R., Iraq

[5] Department of Physics, University of Sargodha, Sargodha 40100, Punjab, Pakistan

[6] Department of Basic Pharmaceutical Sciences, Faculty of Pharmacy, Suleyman Demirel University, Isparta, Türkiye

[7] Faculty of Engineering and Natural Sciences, Bahçeşehir University, Istanbul 34353, Türkiye

[8] Hourani Center for Applied Scientific Research, Al-Ahliyya Amman University, Amman 19328, Jordan

[9] Department of Biosciences, Saveetha School of Engineering, Saveetha Institute of Medical and Technical Sciences, Chennai, 602105, India